Shear-Rate-Dependent Rheology Effects on Mass Transport and Surface Reactions in Biomicrofluidic Devices

Arman Sadeghi
Dept. of Mechanical Engineering, University of Kurdistan, Sanandaj 66177-15175, Iran

Younes Amini
Dept. of Chemical Engineering, Isfahan University of Technology, Isfahan, Iran

Mohammad Hassan Saidi and Hadi Yavari
Center of Excellence in Energy Conversion (CEEC), School of Mechanical Engineering, Sharif University of Technology, Tehran, Iran

DOI 10.1002/aic.14781
Published online March 25, 2015 in Wiley Online Library (wileyonlinelibrary.com)

Consideration is given to shear-rate-dependent rheology effects on mass transport in a heterogeneous microreactor of rectangular cross section, utilizing both numerical and analytical approaches. The carrier liquid obeys the power-law viscosity model and is actuated primarily by an electrokinetic pumping mechanism. It is discovered that, considering the shear-thinning biofluids to be Newtonian fluids gives rise to an overestimation of the saturation time. The degree of overestimation is higher in the presence of large Damkohler numbers and electric double layer thicknesses. It is also increased by the application of a favorable pressure gradient, whereas the opposite is true when an opposed pressure gradient is applied. In addition, a channel of square cross section corresponds to the maximum fluid rheology effects. Finally, the numerical results indicate the existence of a concentration wave when using long channels. This is confirmed by analytical solutions, providing a closed form solution for wave propagation speed. © 2015 American Institute of Chemical Engineers *AIChE J*, 61: 1912–1924, 2015
Keywords: electroosmotic flow, microfluidics, mass transport, surface reaction, nonNewtonian fluids

Introduction

In the recent years, microelectro-mechanical-systems have attracted much attention because of wide practical applications, especially in medical and biological related industries where the microfluidic devices, called lab-on-a-chip (LOC), are becoming more and more popular.[1–5] LOC devices are microscale laboratories on a microchip that can perform clinical diagnoses. The main advantages of these devices are ease of use, speed of analysis, and low sample consumption.[6]

Fluid delivery in LOCs is a challenging task because of small length scales involved. Among various techniques being proposed for fluid pumping in these devices, electroosmosis has been favored due to its advantages over other flow actuation mechanisms. For example, electroosmotic pumps need no moving parts and, as a result, have much simpler design and easier fabrication. Also, precise flow control can be easily achieved by controlling the external electric field.[7]

The term "electroosmosis" refers to the movement of ionized liquids with respect to stationary electrically charged surfaces in the presence of externally applied electric fields. The motion is created by the viscous drag caused by the movement of ions which are experiencing the Coulomb force. The electroosmotic body force is mostly concentrated in a region adjacent to the charged surface known as electric double layer (EDL), shown schematically in Figure 1, where ions are crowded and form an immobile stern layer next to the wall and an outer diffuse mobile layer. It is the motion of the ions within the later that leads to the electroosmotic flow.

Microreactors are one of the essential components of LOCs. As compared with their macroscale counterparts, microreactors have many unique advantages. For example, decrease in the length scales in these devices gives rise to higher amounts of concentration gradient, which is the driving force for mass transport. Moreover, the higher surface to volume ratios at microscale result in higher reaction rates for the systems in which the reaction takes place on the surfaces. In addition, due to the fact that the increase in throughput in microreactors is achieved by a numbering-up approach rather than by scaling-up, higher flexibility is achieved in adapting production rate to varying demands, as a certain number of systems can be switched off or further systems may be simply added to the production plant.[8]

Microreactors are generally divided into homogenous and heterogeneous categories. In the former, reaction takes place within the solution. However, in the heterogeneous reactors, one of the reactants is immobilized on a solid surface and the other reactant is brought close to the surface by the carrier fluid.[9] In both cases, the mass transport process can be

Correspondence concerning this article should be addressed to A. Sadeghi at a.sadeghi@eng.uok.ac.ir.

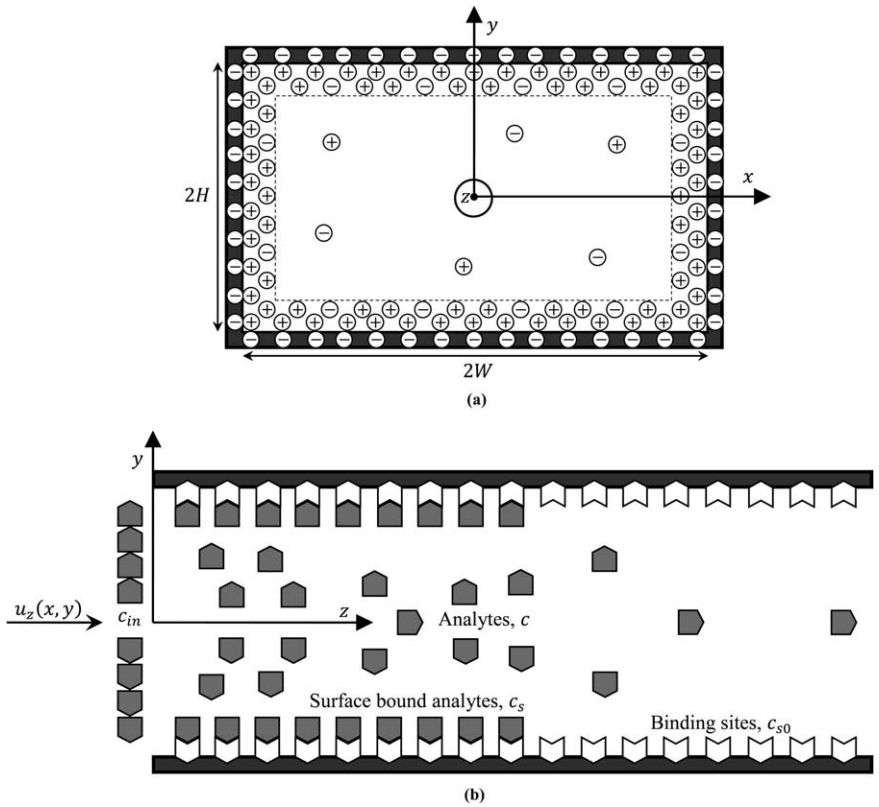

Figure 1. Schematic representation of an electrokinetically driven microreactor.

(a) transverse view including the EDLs between the channel inner wall and the dashed lines and (b) lateral view containing the reactive components.

considered as a subcategory of solute dispersion with chemical reaction. By tracking the literature, one may come across the work of Taylor,[10] as one of the landmark research works on solute dispersion. He provided a description of the cross-sectional area averaged axial convective transport of a passive solute inside a tube in 1953. As then, this method, and also its modified versions developed by other researchers,[11–13] have been called Taylor dispersion theory in the literature. The first work extending the dispersion problem to the situations containing surface reactions was performed by Sankarasubramanian and Gill.[14] They developed analytical solutions for miscible dispersion in laminar flow inside a circular tube in the presence of irreversible first-order reactions at the wall.

Unlike the types of reactions usually presumed in chemical engineering-related research works, the reactions that take place in biological applications are mostly reversible. One of the first attempts in modeling the reversible surface reactions in biological devices was made by Glaser.[15] He numerically studied the kinetics of binding and dissociation between a soluble analyte and an immobilized ligand on or near a surface. This work was followed by a long line of research works on surface reaction in biomicrofluidic devices, utilizing both theoretical[9,16–23] and experimental methods[17,21,23] all considering a pressure driven pumping mechanism. As for electrokinetically driven microdevices, the mass transport studies are more recent and mostly consider an irreversible reaction.[24–35]

The rheological behavior of the biofluids encountered in LOCs may significantly differ from the predictions of the Newton's law of viscosity. Accordingly, any pertinent study should account for this complex rheology, if an accurate modeling is intended to be done. However, no sufficient attention has been given toward the influences of complicated fluid rheology on surface reactions in biomicrofluidic devices. The already available relevant researches, which are very limited in number, provide approximate solutions based on simplifying assumptions such as a constant axial gradient of the concentration[26] and a very small mass-transfer boundary layer[34,35] which limit their applicability range. Moreover, they are dealing with 1-D geometries and have all considered a type of reaction on the surface which is valid only at earlier stages of saturation process in bioreactors. In this work, the gap between full numerical researches pertinent to surface reaction kinetics in bioreactors with Newtonian working fluids and the approximate analyses performed by assuming a shear-rate-dependent rheology is bridged. As the cross section of microchannels made by modern micromachining technologies is usually close to a rectangular shape,[36] a heterogeneous microreactor of this geometry with an electrokinetic flow actuation mechanism is chosen for modeling. The rheological behavior of the working fluid is considered to be described by the power-law viscosity model. The problem is generally handled by means of a finite difference based numerical method for nonuniform grid; however, analytical results, applicable under certain conditions, are also presented. Although the effects of all main parameters on mass transport are being investigated, special attention is given toward the influences of shear-rate-dependent rheology on surface reaction kinetics.

Problem Formulation

The transport of a neutral species in a heterogeneous microreactor of rectangular cross section and its association with the binding sites on the wall are being investigated. A schematic representation of the physical problem along with the coordinate system and the other details is shown in Figure 1. The microreactor enjoys an electrokinetic pumping mechanism. The working fluid is assumed to be a biofluid with its rheological behavior approximately being described by the power-law viscosity model. We also assume that this fluid is of constant thermophysical properties and contains a single symmetric salt dissociating into cationic and anionic species. The zeta potential is also considered constant and uniform which means that the probable alterations of the surface characteristics due to the adsorption–desorption mechanisms is assumed negligible. As the hydrodynamic entry length for an electroosmotic flow is only a small fraction of the channel hydraulic diameter at typical Reynolds numbers,[37] the flow is considered to be fully developed. Due to the symmetry, the analysis is restricted to the first quarter of the channel cross section.

Electrical potential distribution

The electrostatic potential, φ, at any point in the channel will be described by superposition of the externally applied potential, Φ, along the channel axis, and the double layer potential, ψ. Under the hydrodynamically developed conditions $\psi=\psi(x,y)$, so

$$\varphi(x,y,z)=\Phi(z)+\psi(x,y) \tag{1}$$

The electrostatic potential is related to the local net charge density, ρ_e, at certain point in the solution by the Poisson equation[38]

$$\nabla^2\varphi=-\frac{\rho_e}{\varepsilon} \tag{2}$$

where, ε is the permittivity constant of the solution. To evaluate the charge density, first the ionic distributions should be known. As we are dealing with hydrodynamically developed conditions the concentration of ith ionic species is given by the Boltzmann distribution[39]

$$\mathcal{N}_i=\mathcal{N}_0 e^{\left(-\frac{\mathbb{z}_i e\psi}{k_B T}\right)} \tag{3}$$

wherein k_B is the Boltzmann constant, $\mathbb{z}$ denotes the valence number of ion, e is the proton charge, T stands for the absolute temperature, and finally $\mathcal{N}_0$ is the ionic concentration at neutral conditions where $\psi=0$. The charge density for our symmetric solution for which $\mathbb{z}_+=-\mathbb{z}_-=\mathbb{z}$ is, therefore, obtained as

$$\rho_e=\mathbb{z}e(\mathcal{N}_+-\mathcal{N}_-)\ =-2\mathcal{N}_0\mathbb{z}e\sinh\left(\frac{\mathbb{z}e\psi}{k_B T}\right) \tag{4}$$

Introducing the charge density expression into the Poisson equation and performing nondimensionalization result in the following modified version of Eq. 2

$$\frac{\partial^2\psi^*}{\partial x^{*2}}+\frac{\partial^2\psi^*}{\partial y^{*2}}=\mathrm{K}^2\sinh\psi^* \tag{5}$$

where $\psi^*=e\mathbb{z}\psi/k_B T$, $x^*=x/H$, $y^*=y/H$, and $\mathrm{K}=H/\lambda_D$ is the dimensionless Debye-Hückel parameter with $\lambda_D=(2\mathcal{N}_0 e^2\mathbb{z}^2/\varepsilon k_B T)^{-1/2}$ being the Debye length, a measure of the EDL extent. The dimensionless electrical potential Eq. 5 is subject to the following boundary conditions

$$\left.\frac{\partial\psi^*}{\partial x^*}\right|_{x^*=0}=\left.\frac{\partial\psi^*}{\partial y^*}\right|_{y^*=0}=0,\ \ \psi^*|_{x^*=\alpha}=\psi^*|_{y^*=1}=\zeta^* \tag{6}$$

in which $\zeta^*=e\mathbb{z}\zeta/k_B T$ is the dimensionless zeta potential and $\alpha=W/H$ stands for the channel aspect ratio.

Velocity distribution

The momentum exchange through the flow field is governed by the Cauchy equation[40]

$$\rho\frac{D\mathbf{u}}{Dt}=-\nabla p+\nabla\cdot\boldsymbol{\tau}+\mathbf{F} \tag{7}$$

in which ρ denotes the fluid density, p represents the pressure, $\boldsymbol{\tau}$ is the stress tensor, and $\mathbf{F}$ is the body force vector. Here, the body force is given by $\rho_e\mathbf{E}$ with $\mathbf{E}=-\nabla\varphi$ representing the electric field. At the fully developed conditions, the effects of the transverse velocity components are negligible compared with the axial velocity component. This, accompanied by the continuity equation, that is $\nabla\cdot\mathbf{u}=0$, results in a velocity vector of the form $\mathbf{u}=[0,0,u_z(x,y)]$. Therefore, bearing in mind that $D\mathbf{u}/Dt=0$ for a steady fully developed flow, the momentum equation in the axial direction is written as

$$0=-\frac{dp}{dz}+\frac{\partial\tau_{xz}}{\partial x}+\frac{\partial\tau_{yz}}{\partial y}+\rho_e E_z \tag{8}$$

For determining the stress tensor components in Eq. 8, an understanding of the fluid rheology is necessary. Although most biofluids show time-dependent (viscoelastic) flow characteristics, the power-law viscosity and Casson models have shown to be able to provide an approximation of the actual biofluid flow physics, especially in the case of human blood.[26,41] Although the Casson model is usually preferred over the power-law fluid, the latter is utilized here, because of its simplicity and also the ability to fit the experimental data of whole blood and plasma over a wide range of shear rate.[42] The rheology of the power-law fluids is characterized by two parameters namely the flow behavior index, n, and the flow consistency index, m. For a fixed value of n, increasing m will result in the fluid producing more resisting force against the same strain rate. Moreover, the shear-thinning and shear-thickening behaviors are obtained for $n<1$ and $n>1$, respectively and by setting $n=1$ the Newtonian behavior is recovered. Based on this rheology, the components of the shear-stress tensor, appeared in Eq. 8, are of the following forms[43]

$$\tau_{xz}=m\left[\left(\frac{\partial u_z}{\partial x}\right)^2+\left(\frac{\partial u_z}{\partial y}\right)^2\right]^{\frac{n-1}{2}}\frac{\partial u_z}{\partial x} \tag{9}$$

$$\tau_{yz}=m\left[\left(\frac{\partial u_z}{\partial x}\right)^2+\left(\frac{\partial u_z}{\partial y}\right)^2\right]^{\frac{n-1}{2}}\frac{\partial u_z}{\partial y} \tag{10}$$

Similar to that of the electrical potential, the momentum equation is made dimensionless for generalization of the findings. A reference velocity is required for proceeding with this nondimensionalization. This velocity scale here is considered to be the Helmholtz-Smoluchowski electroosmotic velocity, u_{HS}, the maximum possible electroosmotic velocity

for a given electric field which takes the following form for power-law fluids at small zeta potentials[40]

$$u_{HS}=n\lambda_D^{\frac{n-1}{n}}\left(-\frac{\varepsilon\zeta E_z}{m}\right)^{\frac{1}{n}} \tag{11}$$

Substituting τ_{xz} and τ_{yz} from Eqs. 9 and 10 into Eq. 8 and expanding the resultant terms and replacing ρ_e with the righthand side of Eq. 4, the momentum equation in dimensionless form can be written as

$$A_1(x^*,y^*,u^*)\frac{\partial^2 u^*}{\partial x^{*2}}+A_2(x^*,y^*,u^*)\frac{\partial^2 u^*}{\partial y^{*2}} +A_3(x^*,y^*,u^*)\frac{\partial^2 u^*}{\partial x^*\partial y^*}=-\left(\frac{n+1}{n}\right)^n\Gamma-\frac{K^{n+1}}{n^n\zeta^*}\sinh\psi^* \tag{12}$$

where, $u^*=u_z/u_{\mathrm{HS}}$ and the functions $A_{i=1\cdots3}$ are provided in the Appendix. Also, Γ is the velocity scale ratio, defined as

$$\Gamma=\frac{u_{PD}^n}{u_{HS}^n} \tag{13}$$

where, u_{PD} is the maximum velocity of a pressure driven flow of power-law fluids in a slit microchannel with the height of $2H$ which is expressed as[44]

$$u_{PD}^n=\left(\frac{n}{n+1}\right)^n\left(-\frac{1}{m}\frac{dp}{dz}H^{n+1}\right) \tag{14}$$

The momentum equation is subject to the symmetry and no slip boundary conditions that in dimensionless form are written as

$$\left.\frac{\partial u^*}{\partial x^*}\right|_{x^*=0}=\left.\frac{\partial u^*}{\partial y^*}\right|_{y^*=0}=0,\ \ u^*|_{x^*=\alpha}=u^*|_{y^*=1}=0 \tag{15}$$

Concentration distribution

A preliminary understanding of the reaction mechanism is necessary for developing the mass transport equations in a microreactor. In a typical adsorption–desorption mechanism, there are basically three components in the reaction. The first component is the sample being injected into the channel, called analyte, with a concentration of c. The analytes are actually the only component in the buffer fluid. There are also known samples being immobilized on the surface, named binding sites, with a concentration of c_{s0}. Finally, the analytes captured by the binding sites are called surface bound analytes and their concentration is shown by c_{s}. The equation that governs the analytes transport is given as[45]

$$\frac{\partial c}{\partial t}+\nabla\cdot(\mathbf{u}c)=\nabla\cdot(D\nabla c) \tag{16}$$

wherein D is the diffusion coefficient of the analytes. The associated boundary conditions for Eq. 16 include the symmetry conditions at the channel midplanes, the specified inlet conditions, that is the concentration being equal to the injection concentration c_{in}, the vanishing of $\partial^2 c/\partial z^2$ at the outlet, and the equality of the mass flux of the analytes at the wall and the rate of increase in concentration of surface bound analytes, given as

$$\frac{\partial c_s}{\partial t}=-D\nabla c\cdot\hat{\mathbb{n}}=-D\frac{\partial c}{\partial \mathbb{n}} \tag{17}$$

wherein $\mathbb{n}$ is the outward normal direction to the wall and $\hat{\mathbb{n}}$ stands for the unit vector in the direction of $\mathbb{n}$. Using the first-order Langmuir adsorption model, the left hand side of Eq. 17 may also be related to c_{s0}, c_{s}, and the analyte concentration in the channel near the reactive wall, c_{w}, as[20]

$$\frac{\partial c_s}{\partial t}=k_a c_w(c_{s0}-c_s)-k_d c_s \tag{18}$$

where k_{a} and k_{d} are the association and dissociation rates, respectively, thereby assuming a reversible association. The analyte concentration, c, and c_{s} are, therefore, strongly coupled through Eqs. 17 and 18. Assuming a constant diffusivity for the analytes, the dimensionless analyte conservation equation for a steady fully developed flow along with the associated initial and boundary conditions may be written as

$$\frac{\partial\Theta}{\partial t^*}+u^*\frac{\partial\Theta}{\partial z^*}=\frac{\partial^2\Theta}{\partial x^{*2}}+\frac{\partial^2\Theta}{\partial y^{*2}}+\frac{1}{Pe^2}\frac{\partial^2\Theta}{\partial z^{*2}} \tag{19}$$

$$\Theta_{t^*=0}=\left.\frac{\partial\Theta}{\partial x^*}\right|_{x^*=0}=\left.\frac{\partial\Theta}{\partial y^*}\right|_{y^*=0}=\left.\frac{\partial^2\Theta}{\partial z^{*2}}\right|_{z^*=L^*}=0 \tag{20}$$

$$\left.\frac{\partial\Theta}{\partial x^*}\right|_{x^*=\alpha}=-\frac{1}{\epsilon}\frac{\partial\Theta_s}{\partial t^*} \tag{21}$$

$$\left.\frac{\partial\Theta}{\partial y^*}\right|_{y^*=1}=-\frac{1}{\epsilon}\frac{\partial\Theta_s}{\partial t^*} \tag{22}$$

$$\Theta_{z^*=0,t^*>0}=1 \tag{23}$$

wherein

$$\Theta=\frac{c}{c_{in}},\ \ \Theta_s=\frac{c_s}{c_{s0}},\ \ t^*=\frac{Dt}{H^2},\ \ z^*=\frac{z}{HPe},\ \ Pe=\frac{u_{HS}H}{D},\ \ \epsilon=\frac{c_{in}H}{c_{s0}},\ \ L^*=\frac{L}{HPe} \tag{24}$$

where, L denotes the channel length, Pe is the Peclet number, and ϵ is called the relative adsorption capacity. The rate of increase in the concentration of the surface bound analytes, given by Eq. 18, can also be expressed in dimensionless form, as

$$\frac{\partial\Theta_s}{\partial t^*}=\epsilon Da[\Theta_w(1-\Theta_s)-K_D\Theta_s] \tag{25}$$

where the Damkohler number, Da, and the kinetic equilibrium constant, K_{D}, are given as

$$Da=\frac{k_a c_{s0}H}{D},\ \ K_D=\frac{k_d}{k_a c_{in}} \tag{26}$$

Assuming a zero concentration at the time zero, the associated dimensionless initial condition for Eq. 25 is given as

$$\Theta_s|_{t^*=0}=0 \tag{27}$$

The set of coupled governing equations and the initial and boundary conditions are solved utilizing a numerical scheme. The details of calculations are given in numerical procedure section. Once the concentration field is calculated, the quantities of interest can be obtained. One of the main parameters when dealing with biochemical assays is the perimeter averaged concentration of the surface bound analytes. The dimensionless form of this parameter may be written as

$$\Theta_{s,pav}(z^*,t^*)=\frac{\int_0^1\Theta_s|_{x^*=\alpha}dy^*+\int_0^\alpha\Theta_s|_{y^*=1}dx^*}{1+\alpha} \tag{28}$$

Another important parameter is the average value of Θ_s over the entire channel surface which is given as

$$\Theta_{s,av}(t^*)=\frac{\int_0^{L^*}\Theta_{s,pav}dz^*}{L^*} \tag{29}$$

Physical Interpretation of the Dimensionless Parameters

It was found that 10 dimensionless parameters including α, L^*, ζ^*, n, Γ, K, Pe, ϵ, Da, and K_D govern mass transport and surface reaction in a microreactor of rectangular cross section with a power-law working fluid. It is not disadvantageous to briefly discuss the physical significance of these parameters. The first five ones are whether self-explanatory or their physical meanings are already discussed. So we start with K which controls the electroosmotic velocity field. For a small K, the EDL is relatively large and the electroosmotic body force exists in the entire channel. Thus, the velocity variations exist in almost the whole channel domain, giving rise to a nearly parabolic profile. For higher values of K, the EDL is confined to a thin layer near the wall. Accordingly, the velocity variations exist only in this layer and the outside fluid is dragged by the fluid within EDL, creating a plug-like profile.

The Peclet number is defined to be the ratio of the mass-transfer rate due to advection to the rate of transport caused by the diffusion of mass. Accordingly, at smaller values of Pe the diffusion wins and a change in concentration field is propagated into the whole domain. At high Peclet numbers, however, the information is merely transferred by the flow and the disturbances are only felt at downstream locations.

The Damkohler number shows the ratio of the diffusion time scale to the reaction time scale, that is H^2/D to H/k_ac_{s0}. As such, a high value of Da corresponds to a diffusion limited transport. Conversely, when Da is small the transport is limited by the reaction at the surface, leading to a constant concentration profile across the channel.

The relative adsorption capacity, ϵ, denotes the relative density of analytes in the bulk and those located at the fully saturated reacting surface. In other words, it is a measure of surface adsorption capacity relative to the bulk. A small ϵ corresponds to a high relative surface capacity, giving rise to a longer saturation time, and vice versa.

Finally, the kinetic equilibrium constant is a measure of the equilibrium efficiency of the reaction. The ratio of the surface bound analytes at the equilibrium state to the total number of the binding sites is solely dependent on this parameter. In fact, by setting $\partial\Theta_s/\partial t^*=0$ and $\Theta_w=\Theta_{in}=1$, this ratio is readily obtained from Eq. 25 as

$$\Theta_{s,eq}=\frac{c_{s,eq}}{c_{s0}}=\frac{1}{1+K_D} \tag{30}$$

Numerical Procedure

Due to strong gradients of the electrical potential and velocity distributions near the wall, it is necessary to have smaller grid sizes in this region. In addition, at the earlier stages of the saturation process, the axial variation of concentration near the channel inlet is much higher relative to the rest of the channel. Therefore, transformations are used to cluster the grid points near the channel walls and the channel entrance. The x^*, y^*, and z^* coordinates are transformed into $\hat{x}, \hat{y}$, and $\hat{z}$ as[46]

$$\hat{x}=ln\left(\frac{\beta+\frac{x^*}{W^*}}{\beta-\frac{x^*}{W^*}}\right)\Big/ln\left(\frac{\beta+1}{\beta-1}\right) \tag{31}$$

$$\hat{y}=ln\left(\frac{\beta+\frac{y^*}{H^*}}{\beta-\frac{y^*}{H^*}}\right)\Big/ln\left(\frac{\beta+1}{\beta-1}\right) \tag{32}$$

$$\hat{z}=1-ln\left(\frac{\beta_z+1-\frac{z^*}{L^*}}{\beta_z-1+\frac{z^*}{L^*}}\right)\Big/ln\left(\frac{\beta_z+1}{\beta_z-1}\right) \tag{33}$$

where, $H^*=H/H=1$, $W^*=W/H=\alpha$, β is the stretching parameter in the transverse directions, and β_z is the stretching parameter in the axial direction. With this transformation, the dimensionless forms of Eqs. 5, 12, and 19 can be rewritten in terms of $\hat{x}$, $\hat{y}$, and $\hat{z}$ as

$$Q_1^2(\hat{x})\frac{\partial^2\psi^*}{\partial\hat{x}^2}+Q_2(\hat{x})\frac{\partial\psi^*}{\partial\hat{x}}+Q_3^2(\hat{y})\frac{\partial^2\psi^*}{\partial\hat{y}^2}+Q_4(\hat{y})\frac{\partial\psi^*}{\partial\hat{y}}=\mathrm{K}^2\sinh\psi^* \tag{34}$$

$$\begin{aligned}&A_1(\hat{x},\hat{y},u^*)\left[Q_1^2(\hat{x})\frac{\partial^2u^*}{\partial\hat{x}^2}+Q_2(\hat{x})\frac{\partial u^*}{\partial\hat{x}}\right]\\&+A_2(\hat{x},\hat{y},u^*)\left[Q_3^2(\hat{y})\frac{\partial^2u^*}{\partial\hat{y}^2}+Q_4(\hat{y})\frac{\partial u^*}{\partial\hat{y}}\right]\\&+A_3(\hat{x},\hat{y},u^*)\left[Q_1(\hat{x})Q_3(\hat{y})\frac{\partial^2u^*}{\partial\hat{x}\partial\hat{y}}\right]\\&=-\left(\frac{n+1}{n}\right)^n\Gamma-\frac{K^{n+1}}{n^n\zeta^*}\sinh\psi^*\end{aligned} \tag{35}$$

$$\begin{aligned}&\frac{\partial\Theta}{\partial t^*}+u^*Q_5(\hat{z})\frac{\partial\Theta}{\partial\hat{z}}=Q_1^2(\hat{x})\frac{\partial^2\Theta}{\partial\hat{x}^2}+Q_2(\hat{x})\frac{\partial\Theta}{\partial\hat{x}}\\&+Q_3^2(\hat{y})\frac{\partial^2\Theta}{\partial\hat{y}^2}+Q_4(\hat{y})\frac{\partial\Theta}{\partial\hat{y}}\\&+\frac{1}{Pe^2}\left[Q_5^2(\hat{z})\frac{\partial^2\Theta}{\partial\hat{z}^2}+Q_6(\hat{z})\frac{\partial\Theta}{\partial\hat{z}}\right]\end{aligned} \tag{36}$$

where the functions $Q_{i=1\cdots6}$ are provided in the Appendix. The associated boundary conditions are also transformed, accordingly. As the rate Eq. 25 does not include any of the x, y, and z coordinates, it remains unchanged during the transformation process. To achieve a better understanding of the mesh clustering scheme, the physical domain for $\alpha=L^*=1$ with 20 grid points in each direction is drawn in Figure 2 along with the computational space. It can be seen that the distance between two successive grids is reduced by approaching the wall or the entrance.

Applying the central finite difference scheme to the spatial terms and the forward difference scheme to the temporal terms, the discretized forms of Eqs. 34−36, developed for the inner points, along with that of Eq. 25 become

$$k_{0\psi}\psi^*_{i,j}-k_{1\psi}\psi^*_{i+1,j}-k_{2\psi}\psi^*_{i-1,j}=k_{3\psi}\psi^{*g}_{i,j+1}+k_{4\psi}\psi^{*g}_{i,j-1} \tag{37}$$

$$\begin{aligned}&k_{0u}u^*_{i,j}-k_{1u}u^*_{i+1,j}-k_{2u}u^*_{i-1,j}=k_{3u}u^{*g}_{i,j+1}+k_{4u}u^{*g}_{i,j-1}-k_{5u}\\&\left(u^{*g}_{i+1,j+1}-u^{*g}_{i+1,j-1}-u^{*g}_{i-1,j+1}+u^{*g}_{i-1,j-1}\right)+k_{6u}\end{aligned} \tag{38}$$

$$\begin{aligned}&k_{0\Theta}\Theta^{p+1}_{i,j,k}-k_{1\Theta}\Theta^{p+1}_{i+1,j,k}-k_{2\Theta}\Theta^{p+1}_{i-1,j,k}=k_{3\Theta}\Theta^{p+1,g}_{i,j+1,k}\\&+k_{4\Theta}\Theta^{p+1,g}_{i,j-1,k}+k_{5\Theta}\Theta^{p+1,g}_{i,j,k+1}+k_{6\Theta}\Theta^{p+1,g}_{i,j,k-1}+k_{7\Theta}\end{aligned} \tag{39}$$

$$\theta^{p+1}_{s1,j,k}=\frac{\theta^p_{s1,j,k}+\epsilon Da\Delta t^{*p+1}\theta^{p+1,g}_{m+1,j,k}}{1+\epsilon Da\Delta t^{*p+1}\left(K_D+\theta^{p+1,g}_{m+1,j,k}\right)} \tag{40}$$

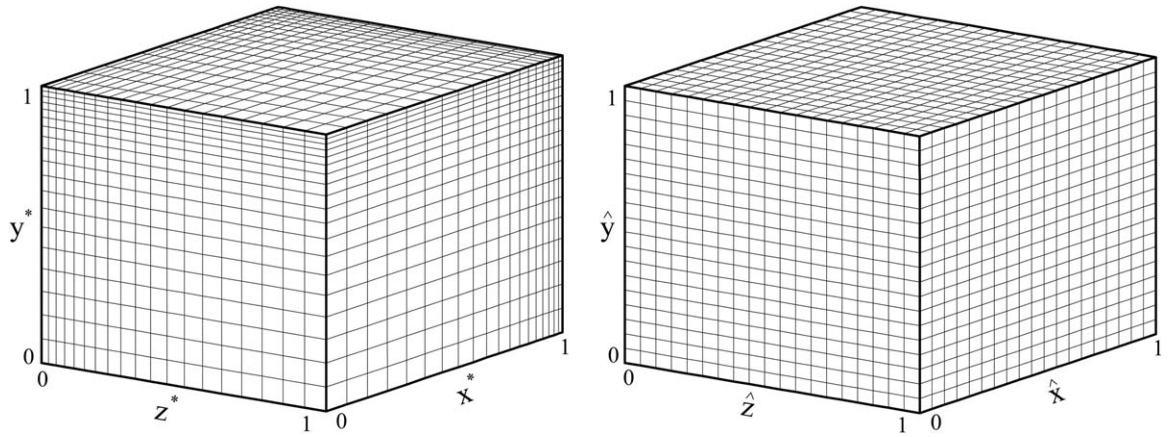

Figure 2. A typical physical domain along with the computational space including details of the grid system used.

$$\theta_{s2,i,k}^{p+1}=\frac{\theta_{s2,i,k}^{p}+\epsilon Da\Delta t^{*p+1}\theta_{i,n+1,k}^{p+1,g}}{1+\epsilon Da\Delta t^{*p+1}\left(K_D+\theta_{i,n+1,k}^{p+1,g}\right)} \tag{41}$$

where, the coefficients k_ψ, k_u, and k_Θ are presented in the Appendix. In addition, indices i, j, and k denote the grid numbers in x, y, and z directions, respectively, while p represents the time step. Superscript g refers to the previous iteration results, while denoting guess values for the first iteration. Note that the parameter $\Lambda_{i,j}=\sinh\psi_{i,j}^{*}/\psi_{i,j}^{*}$ included in $k_{0\psi}$ is appeared in the linearization of the potential equation. For the grids located on the boundaries, appropriate second-order difference equations are used. Equations 40 and 41 show the relevant discretized rate equations for the vertical and horizontal walls represented by the subscripts 1 and 2, respectively. It is noteworthy that separating Θ_s into Θ_{s1} and Θ_{s2} is only for the sake of simplicity in the linkage between the analyte concentration at the wall and that of the surface bound analytes.

The set of algebraic Eqs. 37 is solved by means of tridiagonal matrix algorithm (TDMA). In each iteration, the values of $\Lambda_{i,j}$ are considered to be constant and will be updated in the next iteration after obtaining the new values of $\psi_{i,j}^{*}$ and applying an appropriate over relaxation factor. The procedure continues until the required overall relative error of 10^{-7} is achieved. Afterward, a velocity distribution is guessed and based on which the coefficients containing the guessed values are computed. Equations 38 are then solved and, after applying appropriate under relaxation factors, the new values are used to update the coefficients. This procedure continues until the convergence criterion is satisfied. The velocity magnitudes are used for solving the species transport field. The relevant solution procedure starts by guessing a distribution for Θ at the time step $p+1$. As the values of $\Theta_{i,j,k}^{p}$ are known, they are used as the first guess. The values of Θ_{s}^{p+1} are then being evaluated by means of Eqs. 40 and 41. The boundary conditions of the analyte concentration in the fluid can now be completed by substituting the computed values of Θ_{s}^{p+1} into the discretized forms of Eqs. 21 and 22. The set of discretized governing equations for Θ is then solved by means of the TDMA solver. After a complete sweeping of the domain, an appropriate under relaxation factor is applied and the new data are then used as a new guess to recalculate Θ_{s}^{p+1}. The procedure is going on until the required overall relative error of 10^{-7} is achieved.

Due to different distributions of the gradients in concentration and velocity fields, it is necessary to use different values of β for these fields. Moreover, the required number of the grid points to get grid independent results is much smaller for the concentration field as compared with the velocity field. Hence, it is necessary to transfer the velocity magnitudes into the simulation domain of the concentration field. We use the bilinear interpolation scheme for data transfer between the fields. For the concentration field, the values of $\beta=1.1$ and $\beta_z=1.2$ are considered. For the electrical potential and velocity fields, however, the appropriate β depends on K because the gradients are higher near the wall for higher values of this parameter. Accordingly, the associated value of β should more and more approach unity by increasing K. The dependency of β on K for the electrical potential and velocity fields here is considered to be $\beta=1+1/3K$. Finally, the ratio of the two successive time steps $\Delta t^{*p+1}/\Delta t^{*p}$ was varied between 1 and 1.1 and it was found that a ratio of 1.03 provides the most accurate results.

Method Validation

To ensure that the obtained results are not dependent on the grid size and the time step, extensive analyses were done, revealing that utilizing 80 time steps from the injection to saturation along with $40\times40\times80$ grids in x, y, and z directions, respectively, results in sufficiently accurate results. For validation of the numerical solution, a comparison is made between the present results and those of reaction limited conditions for which an analytical solution is possible. Given the physical meaning of the Damkohler number discussed before, at the limit $Da\rightarrow0$ there is no resistance to mass transfer and the transport is purely reaction limited. Hence, the analyte concentration at any point in the channel instantaneously becomes the same as the injection concentration, resulting in a dimensionless concentration of $\Theta=1$. Under such conditions, the dimensionless rate Eq. 25 becomes

$$\frac{d\Theta_{s,rl}}{dt^{*}}=\epsilon Da\left[1-(1+K_D)\Theta_{s,rl}\right] \tag{42}$$

which can readily be solved to yield

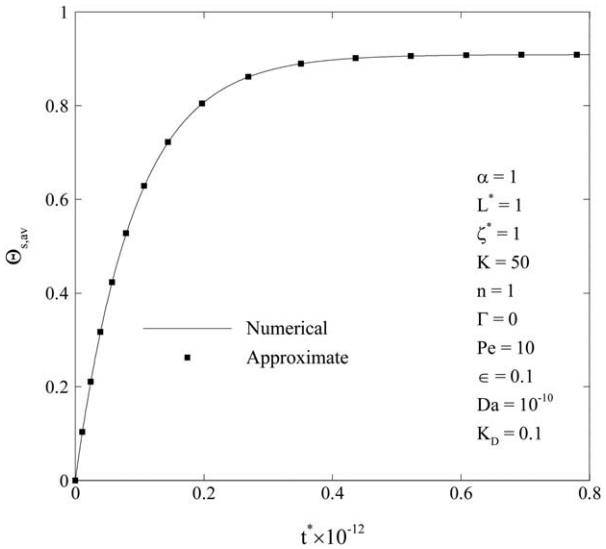

Figure 3. Comparison between the numerically computed values of $\Theta_{s,av}$ and those predicted by the reaction limited solution, given by Eq. 43.

$$\Theta_{s,rl}=\frac{1-e^{-\epsilon Da(1+K_D)t^*}}{1+K_D} \tag{43}$$

Figure 3 compares the numerically computed values of $\Theta_{s,av}$ and those predicted by the reaction limited solution for a small Damkohler number of $Da=10^{-10}$, revealing an excellent agreement between them.

Results and Discussion

Ten governing parameters are too many for performing a parametric study including all of their effects on the surface reaction kinetics. Therefore, we only vary the ones which are of highest interest and fix the others at reasonable values. Table 1, presenting the practical ranges of the physical parameters, is a useful guide in this respect. Considering these data, the parameters ζ^*, ϵ, Pe, and K_D are fixed at moderate values of 4, 0.1, 10, and 0.1, respectively. In addition, unless otherwise is stated, the parameter set of $\alpha=2$, $L^*=1$, $K=10$, $n=0.7$, $\Gamma=0$, and $Da=10$ is considered.

We begin the presentation of the results with illustrating the profiles of the dimensionless analyte concentration at different values of the Damkohler number and the normalized time t^*/t^*_{eq} in Figure 4. This variant of the dimensionless time is used to pave the way for a better judgment of the Damkohler number effects. As observed from the figure, for a given normalized time, a more uniform profile is achieved by decreasing Da. As mentioned previously, this is because of increasing the diffusion effects. The figure also reveals that the maximum of the analyte concentration profile occurs at the centerline where the surface effects are minimum. The analytes moving near the corner have a small velocity and are exposed to reaction from both the vertical and horizontal walls. Hence, most analytes will be captured by the binding sites on the walls, resulting in the minimum analyte concentration in the flow field, as observed in the figure.

Figure 5 depicts a typical distribution of Θ_s. As expected, the concentration of the surface bound analytes is a decreasing function of the axial coordinate. At the channel inlet, Θ_s is independent of y^*, because of the uniformity of the analyte concentration. For other axial positions, Θ_s is decreased by approaching the corner, due to smaller availabilities of the analytes at higher values of y^*.

Table 1. Practical Ranges of Physical Parameters

Parameter	Value
Flow behavior index n[26,42,47]	0.4−1.2
Half channel height H[20]	0.5−25 μm
Half channel width W[20]	10−250 μm
Channel length L[20]	0.1−2 mm
Debye length λ_D[48]	1−100 nm
Zeta potential ζ[49]	5−245 mV
Electric field E_z[48]	1−100 kVm^{-1}
Diffusivity D[20]	43−100 μm^{2}s^{-1}
Injection concentration c_{in}[20]	0.1 μM
Concentration of binding sites c_{s0}[20]	8−70 fmol mm^{-2}
Association rate k_a[20]	1.2×10^5−2.4×10^5 M^{-1}s^{-1}
Dissociation rate k_d[20]	0−3.5×10^{-3}s^{-1}

The time evolution of $\Theta_{s,\mathrm{pav}}$ is shown in Figure 6. At the beginning, the analytes merely exist near the entrance; hence, the reaction only takes place at this region. Due to the high availability of the binding sites, the reaction process occurs at a high rate, giving rise to the depletion of the solution. As the time is passed, the reaction rate decreases in the channel entrance. Besides, the analytes have sufficient time to reach higher axial positions. Accordingly, the region of reaction is extended to the downstream. At higher time scales, the upstream region is saturated; under these conditions, the rate of binding is balanced with the dissociation rate and, hence, the inlet analytes are totally transferred downstream.

At higher channel lengths, the entrance region may reach saturation while the reaction is practically not started at the channel outlet. Such a situation can be observed in Figure 7 which depicts the profiles of $\Theta_{s,\mathrm{pav}}$ for $L^*=10$. In these cases, a concentration wave is formed which propagates into the channel at a constant velocity smaller than the fluid mean velocity. The speed of the wave normalized with u_{HS} is calculated to be about 0.070. The exact value of this speed can be obtained by an analytical treatment of the governing equations. The analysis starts by integrating Eq. 19 over the dimensionless channel cross sectional area, $\mathbb{A}^*$, to yield

$$\frac{\partial\Theta_{csa}}{\partial t^*}+u^*_m\frac{\partial\Theta_b}{\partial z^*}=\frac{1}{\alpha}\int_{\mathbb{A}^*}\nabla^{*2}\Theta d\mathbb{A}^*+\frac{1}{Pe^2}\frac{\partial^2\Theta_{csa}}{\partial z^{*2}} \tag{44}$$

where the subscript csa stands for the cross-sectional average, u^*_{m} denotes the dimensionless mean velocity, and Θ_b is the velocity averaged (bulk mean) analyte concentration. It should be pointed out that, here and in what follows, the dimensionless Del operator, $\nabla^*=H\nabla$, is assumed to operate only in x-y plane. Making use of the divergence theorem and the dimensionless form of Eq. 17, the first term on the right side of Eq. 44 may be rewritten as

$$\frac{1}{\alpha}\int_{\mathbb{A}^*}\nabla^{*2}\Theta d\mathbb{A}^*=\frac{1}{\alpha}\int_{\mathbb{P}^*}\nabla^*\Theta\cdot\hat{\mathbb{n}}d\mathbb{P}^*=-\frac{1}{\epsilon\alpha}\int_{\mathbb{P}^*}\frac{\partial\Theta_s}{\partial t^*}d\mathbb{P}^* \tag{45}$$

where $\mathbb{P}^*$ stands for the dimensionless channel perimeter. Equation 44 is, therefore, modified into the following form, after taking advantage of Eq. 28

$$\frac{\partial\Theta_{csa}}{\partial t^*}+u^*_m\frac{\partial\Theta_b}{\partial z^*}=-\frac{1+1/\alpha}{\epsilon}\frac{\partial\Theta_{s,pav}}{\partial t^*}+\frac{1}{Pe^2}\frac{\partial^2\Theta_{csa}}{\partial z^{*2}} \tag{46}$$

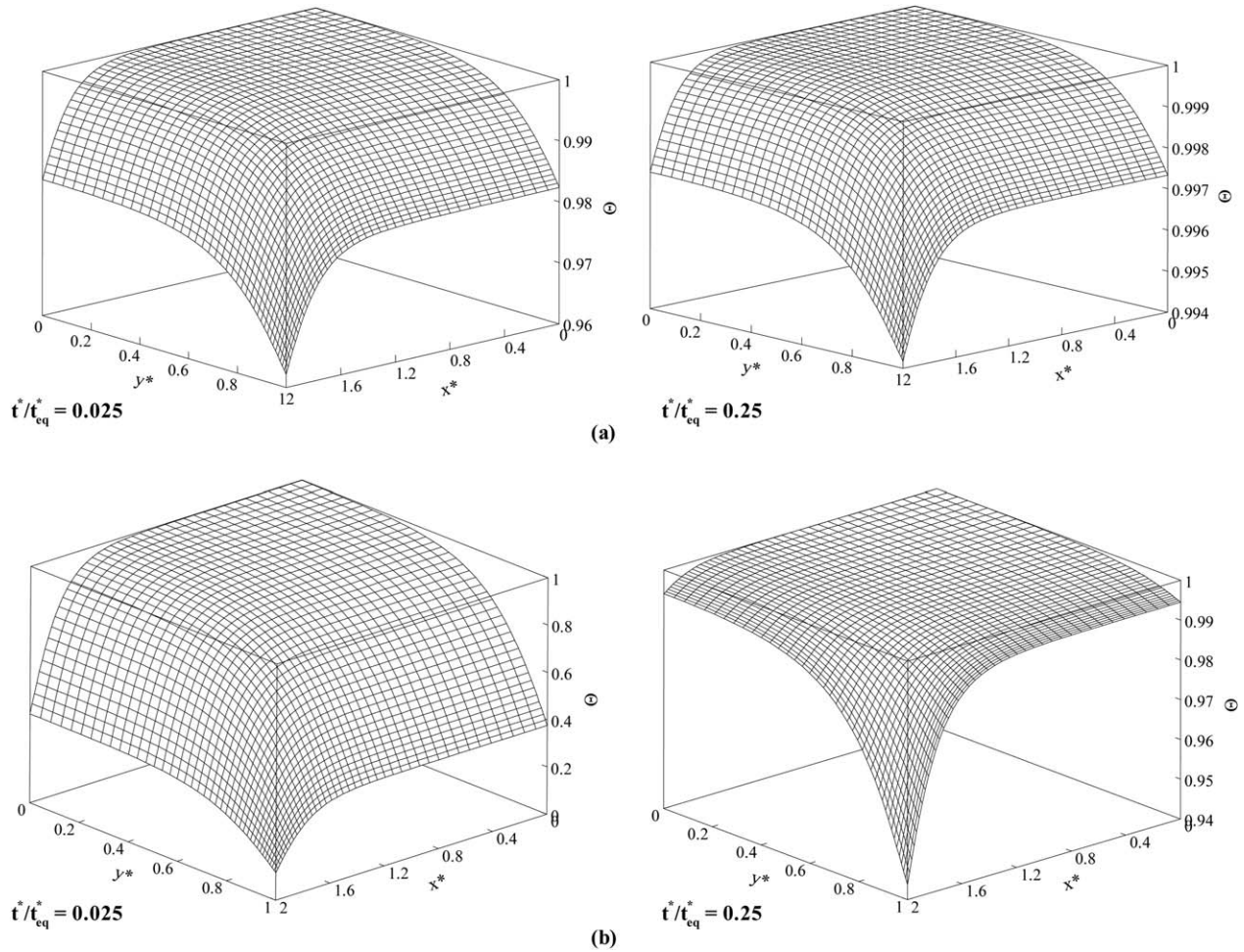

Figure 4. Profiles of Θ at $z^* = 0.0355$ for different values of t^*/t^*_{eq} (a) $Da = 0.1$ and (b) $Da = 10$.

We now fix the coordinate system to the wave front by applying a variable change of the form

$$\mathcal{Z} = z^* - \frac{u_{eff}}{u_{HS}} t^* = z^* - u^*_{eff} t^* \tag{47}$$

wherein u_{eff} is the effective propagation velocity. Based on this new coordinate system, Eq. 46 becomes

$$u^*_{eff} \frac{d\Theta_{csa}}{d\mathcal{Z}} - u^*_m \frac{d\Theta_b}{d\mathcal{Z}} + \frac{1+1/\alpha}{\epsilon} u^*_{eff} \frac{d\Theta_{s,pav}}{d\mathcal{Z}} + \frac{1}{Pe^2} \frac{d^2\Theta_{csa}}{d\mathcal{Z}^2} = 0 \tag{48}$$

Integrating Eq. 48 from $-\infty$ to $+\infty$ with the consideration of the associated boundary conditions given as

$$\Theta_b|_{\mathcal{Z}\to-\infty} = \Theta_{csa}|_{\mathcal{Z}\to-\infty} = 1,\ \Theta_{s,pav}|_{\mathcal{Z}\to-\infty} = \frac{1}{1+K_D},\ \left.\frac{d\Theta_{csa}}{d\mathcal{Z}}\right|_{\mathcal{Z}\to-\infty} = 0 \tag{49}$$

$$\Theta_b|_{\mathcal{Z}\to+\infty} = \Theta_{csa}|_{\mathcal{Z}\to+\infty} = \Theta_{s,pav}\Big|_{\mathcal{Z}\to+\infty} = 0,\ \left.\frac{d\Theta_{csa}}{d\mathcal{Z}}\right|_{\mathcal{Z}\to+\infty} = 0$$

results in the following expression for u^*_{eff}

$$u^*_{eff} = \left[1 + \frac{1+1/\alpha}{\epsilon(1+K_D)}\right]^{-1} u^*_m \tag{50}$$

The effective propagation velocity u_{eff} is, therefore, not dependent on the Peclet number. In fact, when normalizing with the mean velocity, it is a function of only three parameters comprising α, ϵ, and K_D that govern the adsorption kinetics at these conditions in a manner that higher values of them result in a faster saturation. This is why the wave propagation speed is an increasing function of all of these parameters. Equation 50 predicts a dimensionless propagation velocity of 0.0703 for the parameter set of Figure 7, a value very close to the numerical result. Moreover, the ratio $u_{\text{eff}}/u_{\text{m}}$ becomes 0.068, revealing that the propagation velocity is about 15 times smaller than the fluid mean velocity.

The effects of the power-law rheology on the saturation process for two different values of *Da* are shown in Figure 8. A decrease in *n* leads to a smaller resistance against flow and, accordingly, higher velocities. Therefore, the analytes travel along the channel more quickly, resulting in more availability of analytes adjacent to the surface. This paves the way for a faster reaction and, ultimately, a shorter saturation time, as seen in the figure. Comparing the two sections of Figure 8 leads one to the conclusion that the rheology effects are pronounced by increasing the Damkohler number. This is not surprising by referring to the physical interpretation of *Da*. At lower values of *Da*, the shortage of analytes near the wall is compensated by the diffusion mechanism. However, at higher Damkohler numbers, the diffusion mechanism is very slow and the analytes are mainly conveyed by the flow, leading to higher effects of the velocity pattern on the saturation process.

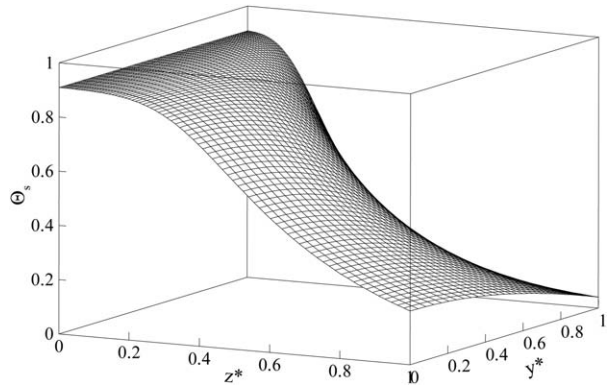

Figure 5. Distribution of Θ_s at the vertical wall for $t^* = 10.5$.

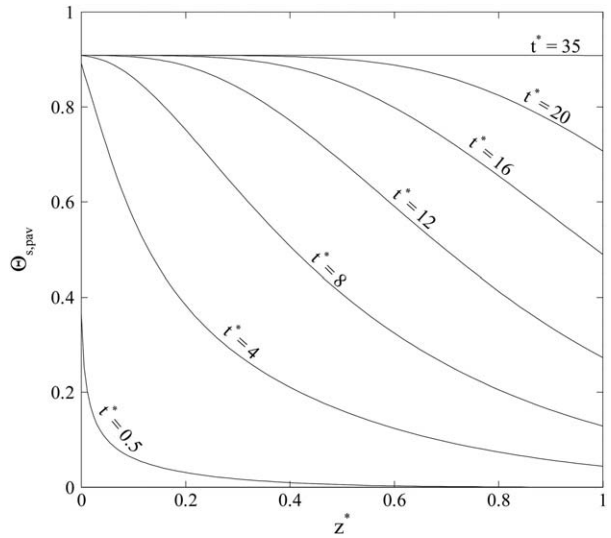

Figure 6. Time evolution of $\Theta_{s,pav}$.

Besides the Damkohler number, there are other parameters that affect the extent to which the fluid rheology can influence the saturation process. One of these parameters is the

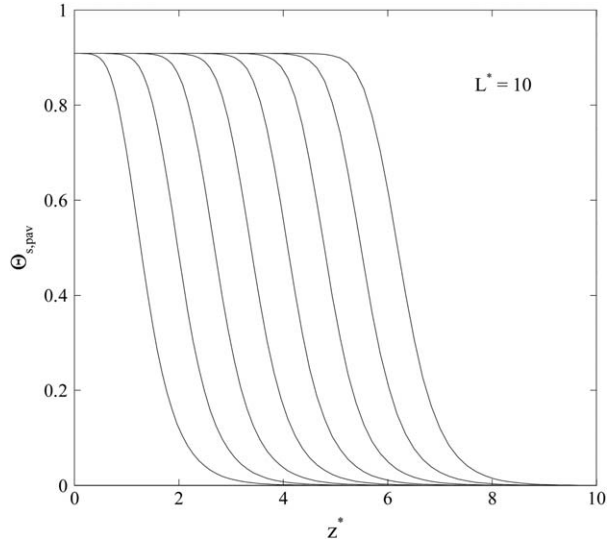

Figure 7. Profiles of $\Theta_{s,pav}$ for equidistant moments in time between $t^* = 20$ to $t^* = 90$.

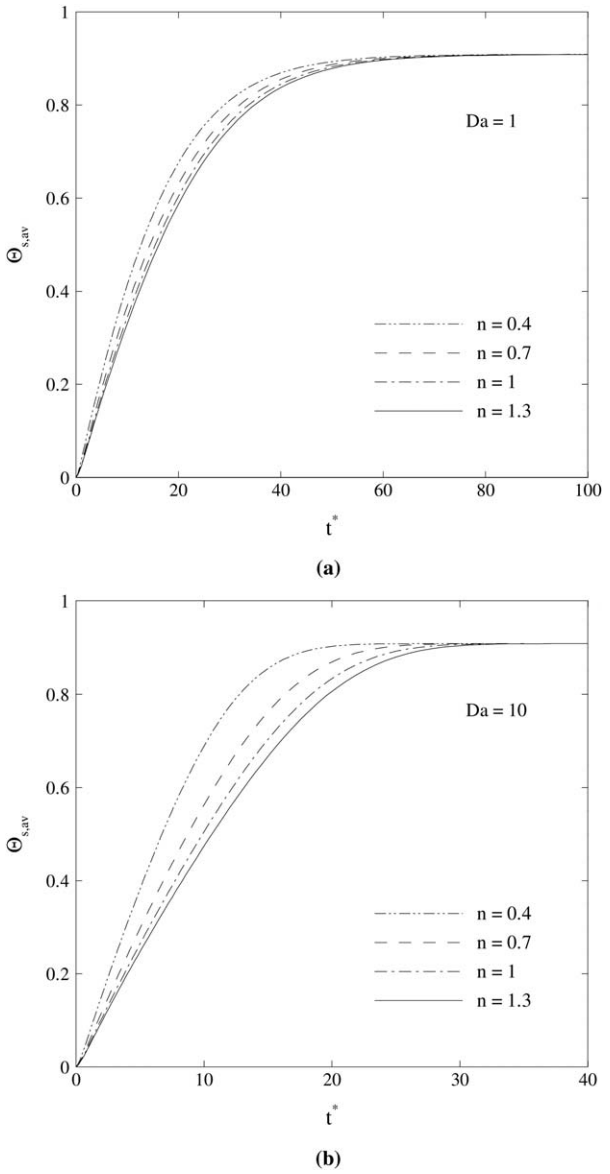

Figure 8. Effects of fluid rheology on profiles of $\Theta_{s,av}$ vs. t^* for (a) $Da = 1$ and (b) $Da = 10$.

EDL thickness that is here studied through K. As noted previously, by increasing this parameter a more plug-like velocity profile is achieved. This velocity profile is not much affected by the fluid rheology and, hence, the effects of the flow behavior index on surface reaction kinetics is decreased at higher values of K. This is observed in Figure 9 that presents the graphs of $\Theta_{s,av}$ vs. t^* for different values of n and K. Conversely, the more concentration of the electroosmotic body force near the wall gives rise to higher velocities in this region for the same values of n. This, ultimately, results in faster reactions for smaller EDL thicknesses, as observed in Figure 9.

Figure 10 shows the interactive impacts of the channel aspect ratio and flow behavior index on the surface reactions. It can be seen that, a higher α is accompanied by a smaller saturation time. The first reason of this trend is higher volume to surface ratios at higher values of α for a given channel height, which, ultimately, lead to a higher availability of analytes, because the amount of the injected analytes is

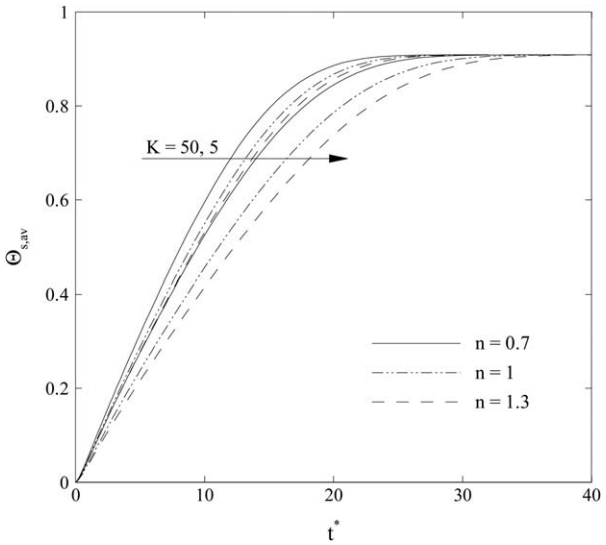

Figure 9. Effects of flow behavior index on profiles of $\Theta_{s,av}$ vs. t^* for two different values of EDL thickness.

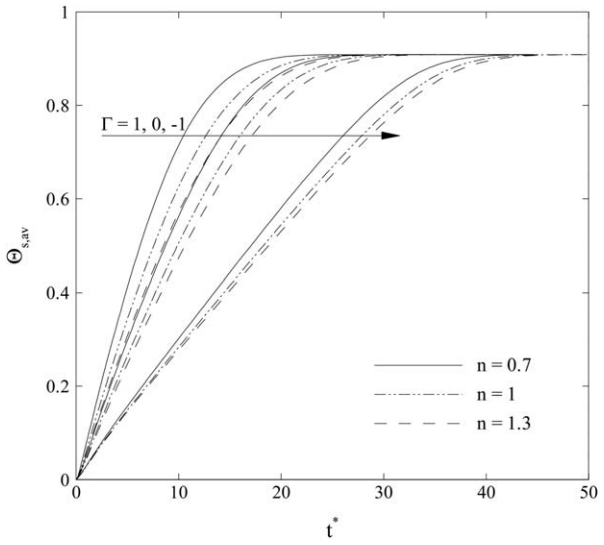

Figure 11. Effects of flow behavior index on profiles of $\Theta_{s,av}$ vs. t^* for two different velocity scale ratios.

proportional to the channel volume. In addition, the rate of reaction near the corners is slower as compared with the other regions because of the analyte shortage which itself is a result of small velocities. As the maximum corner effects are associated with a channel of square cross section, an increase in α gives rise to smaller corner effects, thereby increasing the reaction rate. Figure 10 also reveals that the power-law rheology effects on the saturation process are maximal for a channel of square shape, an expected trend considering the associated maximum corner effects.

The last illustration being presented, that is Figure 11, is pertinent to the velocity scale ratio effects on the saturation process at different values of n. The reaction rate is found to be an increasing function of Γ. This is expected, due to the fact that, a higher value of this parameter corresponds to higher velocities. The more influence of the pressure gradient for a negative Γ may be attributed to the distortion of the velocity profile in the presence of an opposed pressure gradient. It is also found from Figure 11 that, the rheology effects in the case of fluids having shear-rate-dependent behavior are pronounced by applying a favorable pressure gradient, corresponding to a positive value of the velocity scale ratio, whereas the opposite is true when the flow is subject to an opposed pressure gradient.

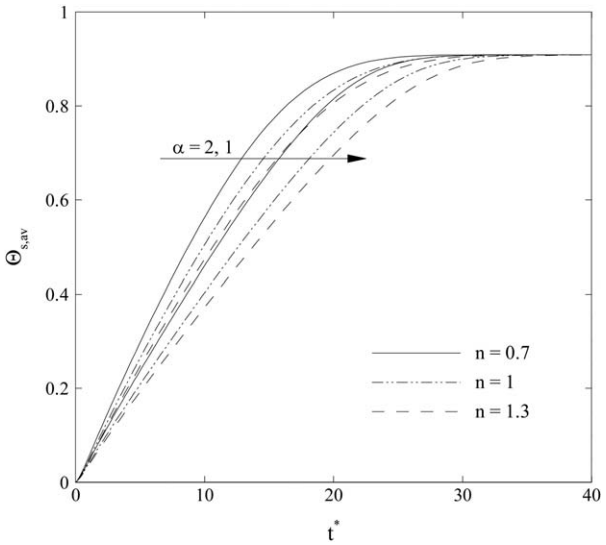

Figure 10. Effects of flow behavior index on profiles of $\Theta_{s,av}$ vs. t^* for two different channel aspect ratios.

Conclusions

The shear-rate-dependent rheology effects on mass transport and surface reactions in a heterogeneous microchannel of rectangular cross section were studied in this article. The carrier liquid, considered to be a power-law fluid, was assumed to be actuated by a combined action of electroosmotic and pressure forces. The problem was handled by a finite difference based numerical approach with a grid system appropriately clustered in high gradient regions. When possible, analytical solutions were also presented. The results revealed that utilizing a fluid with a smaller value of the flow behavior index leads to faster reactions; this means that, for shear-thinning biofluids such as blood, one may expect much shorter saturation times. The power-law rheology effects were found to be significantly pronounced in the presence of large Damkohler numbers and EDL thicknesses. It was also observed that any deviation of the channel cross section from a square shape gives rise to the depletion of fluid characteristics impacts on the mass transport phenomena. Moreover, when a favorable pressure gradient is applied along the channel, the dependence of surface reaction kinetics on the fluid rheology is increased, whereas the opposite is true for an opposed pressure gradient. Last but not least, a concentration wave may be created for sufficiently long channels; utilizing an analytical approach, it was shown that, when normalized with the fluid mean velocity, the wave propagation speed depends only on three parameters comprising the channel aspect ratio, the kinetic equilibrium constant, and the relative adsorption capacity.

Acknowledgment

The first author sincerely thanks Iran's National Elites Foundation (INEF) for its supports during the course of this work.

Notation

$\mathbb{A}$ = channel cross sectional area, m^2
c = analyte concentration, m^{-3}
c_{in} = injection concentration, m^{-3}
c_s = concentration of surface bound analytes, m^{-2}
c_{s0} = concentration of the binding sites, m^{-2}
D = diffusion coefficient, $m^2 s^{-1}$
Da = Damkohler number, $=k_a c_{s0} H/D$
e = proton charge, C
$\mathbf{E}$ = electric field, V m^{-1}
E_z = electric field in axial direction, V m^{-1}
$\mathbf{F}$ = body force vector, N m^{-3}
H = half channel height, m
k_a = association rate, m^3 s^{-1}
k_B = Boltzmann constant, J K^{-1}
k_d = dissociation rate, s^{-1}
K_D = kinetic equilibrium constant, $= k_d/k_a c_{in}$
L = channel length, m
m = flow consistency index, Pa s^n
n = flow behavior index
$\mathcal{N}_i$ = concentration of ith ionic species, m^{-3}
$\mathcal{N}_0$ = ionic concentration at neutral conditions, m^{-3}
$\mathbb{n}$ = outward normal direction to the wall, m
$\hat{\mathbb{n}}$ = unit vector in the direction of $\mathbb{n}$
p = pressure, Pa
$\mathbb{P}$ = channel perimeter, m
Pe = Peclet number, $= u_{HS} H/D$
t = time, s
T = temperature, K
$\mathbf{u}$ = velocity vector, m s^{-1}
u_{eff} = effective propagation velocity, m s^{-1}
u_{HS} = Helmholtz-Smoluchowski velocity, m s^{-1}
u_{PD} = pressure driven velocity, m s^{-1}
u_z = axial velocity, m s^{-1}
W = half channel width, m
x, y, z = coordinates, m
$\mathbb{z}$ = valence number of ions in solution
$\mathcal{Z}$ = dimensionless coordinate fixed to the wave front, $= z^* - u_{eff}^* t^*$

Greek letters

α = channel aspect ratio, $= W/H$
β, β_z = stretching parameters
Γ = velocity scale ratio, $= u_{PD}^n / u_{HS}^n$
ε = permittivity of medium, $CV^{-1}m^{-1}$
ϵ = relative adsorption capacity, $= c_{in} H/c_{s0}$
ζ = zeta potential, V
Θ = dimensionless concentration of analytes, $= c/c_{in}$
Θ_s = dimensionless concentration of surface bound analytes, $= c_s/c_{s0}$
κ = dimensionless Debye-Hückel parameter, $= H/\lambda_D$
λ_D = Debye length, m
ρ = mass density, kg m^{-3}
ρ_e = electrical charge density, C m^{-3}
τ = stress tensor component, Pa
$\boldsymbol{\tau}$ = stress tensor, Pa
φ = electrostatic potential, V
Φ = externally imposed electrostatic potential, V
ψ = EDL electrostatic potential, V

Subscripts

av = average
b = bulk mean
csa = cross sectional average
eq = equilibrium
i, j, k = grid numbers
m = mean
pav = perimeter averaged
rl = reaction limited
w = near reactive wall

Superscripts

g = guess value
p = time step
$*$ = dimensionless variable
$\hat{}$ = transferred variable

Literature Cited

1. Elvira KS, i Solvas XC, Wootton RCR, deMello AJ. The past, present and potential for microfluidic reactor technology in chemical synthesis. *Nat Chem*. 2013;5(11):905–915.
2. Meier M, Sit R, Pan W, Quake SR. High-performance binary protein interaction screening in a microfluidic format. *Anal Chem*. 2012; 84(21):9572–9578.
3. Martin L, Meier M, Lyons SM, Sit RV, Marzluff WF, Quake SR, Chang HY. Systematic reconstruction of RNA functional motifs with high-throughput microfluidics. *Nat Methods*. 2012;9(12):1192–1194.
4. Lorthongpanich C, Cheow LF, Balu S, Quake SR, Knowles BB, Burkholder WF, Solter D, Messerschmidt DM. Single-cell DNA-methylation analysis reveals epigenetic chimerism in preimplantation embryos. *Science* 2013;341:1110–1112. zaq no=
5. Pommella A, Tomaiuolo G, Chartoire A, Caserta S, Toscano G, Nolan SP, Guido S. Palladium-N-heterocyclic carbene (NHC) catalyzed C-N bond formation in a continuous flow microreactor. Effect of process parameters and comparison with batch operation. *Chem Eng J*. 2013;223:578–583.
6. Babaie A, Saidi MH, Sadeghi A. Heat transfer characteristics of mixed electroosmotic and pressure driven flow of power-law fluids in a slit microchannel. *Int J Therm Sci*. 2012;53:71–79.
7. Sadeghi A, Saidi MH. Viscous dissipation effects on thermal transport characteristics of combined pressure and electroosmotically driven flow in microchannels. *Int J Heat Mass Transfer*. 2010; 53(19–20):3782–3791.
8. Ehrfeld W, Hessel V, Löwe H. *Microreactors: New Technology for Modern Chemistry*. Weinheim: Wiley, 2000.
9. Jomeh S, Hoorfar M. Numerical modeling of mass transport in microfluidic biomolecule-capturing devices equipped with reactive surfaces. *Chem Eng J*. 2010;165(2):668–677.
10. Taylor G. Dispersion of soluble matter in solvent flowing slowly through a tube. *Proc R Soc Lond Ser A*. 1953;219(1137):186–203.
11. Aris R. On the dispersion of a solute in a fluid flowing through a tube. *Proc R Soc Lond Ser A*. 1956;235:67–77.
12. Pagitsas M, Nadim A, Brenner H. Projection operator analysis of macrotransport processes. *J Chem Phys*. 1986;84:2801–2807.
13. Mercer GN, Roberts AJ. A centre manifold description of contaminant dispersion in channels with varying flow properties. *SIAM J Appl Math*. 1990;50:1547–1565.
14. Sankarasubramanian R, Gill WN. Unsteady convective diffusion with interphase mass transfer. *Proc R Soc Lond Ser A*. 1973;333:115–132.
15. Glaser RW. Antigen-antibody binding and mass transport by convection and diffusion to a surface: a two-dimensional computer model of binding and dissociation kinetics. *Anal Biochem*. 1993;213(1):152–161.
16. Dutta D. Solutal transport in rectangular nanochannels under pressure-driven flow conditions. *Microfluid Nanofluid*. 2011;10(3):691–696.
17. Roy B, Das T, Maiti TK, Chakraborty S. Effect of fluidic transport on the reaction kinetics in lectin microarrays. *Anal Chim Acta*. 2011; 701(1):6–14.
18. Hansen R, Bruus H, Callisen TH, Hassager O. Transient convection, diffusion, and adsorption in surface-based biosensors. *Langmuir*. 2012;28(19):7557–7563.
19. Yarmush ML, Patankar DB, Yarmush DM. An analysis of transport resistance in the operation of BIAcore(TM); Implications for kinetic studies of biospecific interactions. *Molecular Immunology*. 1996; 33(15):1203–1214.
20. Gervais T, Jensen KF. Mass transport and surface reactions in microfluidic systems. *Chem Eng Sci*. 2006;61(4):1102–1121.
21. Parsa H, Chin CD, Mongkolwisetwara P, Lee BW, Wang JJ, Sia SK. Effect of volume- and time-based constraints on capture of analytes in microfluidic heterogeneous immunoassays. *Lab Chip*. 2008; 8(12):2062–2070.
22. Squires TM, Messinger RJ, Manalis SR. Making it stick: convection, reaction and diffusion in surface-based biosensors. *Nat Biotechnol*. 2008;26(4):417–426.
23. Mocanu D, Kolesnychenko A, Aarts S, Troost-Dejong A, Pierik A, Vossenaar E, Stapert H. Mass transfer effects on DNA hybridization in a flow-through microarray. *J Biotechnol*. 2009;139(2):179–185.

24. Tang GY, Yang C, Chai CK, Gong HQ. Numerical analysis of the thermal effect on electroosmotic flow and electrokinetic mass transport in microchannels. *Anal Chim Acta*. 2004;507(1):27–37.
25. Das S, Das T, Chakraborty S. Analytical solutions for the rate of DNA hybridization in a microchannel in the presence of pressure-driven and electroosmotic flows. *Sensor Actuat B Chem*. 2006; 114(2):957–963.
26. Das S, Chakraborty S. Analytical solutions for velocity, temperature and concentration distribution in electroosmotic microchannel flows of a non-Newtonian bio-fluid. *Anal Chim Acta*. 2006;559(1):15–24.
27. Das S, Das T, Chakraborty S. Modeling of coupled momentum, heat and solute transport during DNA hybridization in a microchannel in the presence of electro-osmotic effects and axial pressure gradients. *Microfluid Nanofluid. 2006;*2(1):37–49.
28. Dutta D. Electroosmotic transport through rectangular channels with small zeta potentials. *J. Colloid Interface Sci*. 2007;315(2):740–746.
29. Hu G, Gao Y, Li D. Modeling micropatterned antigen-antibody binding kinetics in a microfluidic chip. *Biosens Bioelectron*. 2007;22(7): 1403–1409.
30. Subramaniam K, Chakraborty S. A semi-analytical model for species transport in combined electroosmotic and pressure driven microflows with surface adsorption-desorption reactions. *Microfluid Nanofluid*. 2011;10(4):821–829.
31. Sharma H, Vasu N, De S. Mass transfer during catalytic reaction in electroosmotically driven flow in a channel microreactor. *Heat Mass Transfer*. 2011;47(5):541–550.
32. Vennela N, Bhattacharjee S, De S. Sherwood number in porous microtube due to combined pressure and electroosmotically driven flow. *Chem Eng Sci*. 2011;66(24):6515–6524.
33. Vennela N, Mondal S, De S, Bhattacharjee S. Sherwood number in flow through parallel porous plates (Microchannel) due to pressure and electroosmotic flow. *AIChE J*. 2012;58(6):1693–1703.
34. Mondal S, De S. Mass transport in a porous microchannel for non-Newtonian fluid with electrokinetic effects. *Electrophoresis*. 2013; 34(5):668–673.
35. Mondal S, De S. Effects of non-Newtonian power law rheology on mass transport of a neutral solute for electro-osmotic flow in a porous microtube. *Biomicrofluidics*. 2013;7(4).
36. Stone HA, Stroock AD, Ajdari A. Engineering flows in small devices: microfluidics toward a lab-on-a-chip. *Ann Rev Fluid Mech*. 2004;36:381–411.
37. Yang RJ, Fu LM, Hwang CC. Electroosmotic Entry Flow in a Microchannel. *J Colloid Interface Sci*. 2001;244(1):173–179.
38. Masliyah JH, Bhattacharjee S. *Electrokinetic and Colloid Transport Phenomena*, 1st ed. NJ: Wiley, 2006.zaq no=
39. Yang C, Li D, Masliyah JH. Modeling forced liquid convection in rectangular microchannels with electrokinetic effects. *Int J Heat Mass Transfer*. 1998;41(24):4229–4249.
40. Zhao C, Zholkovskij E, Masliyah J, Yang C. Analysis of electroosmotic flow of power-law fluids in a slit microchannel. *J Colloid Interface Sci*. 2008;326(2):503–510.
41. Chakraborty S. Electroosmotically driven capillary transport of typical non-Newtonian biofluids in rectangular microchannels. *Anal Chim Acta*. 2007;605(2):175–184.
42. Sharma K, Bhat SV. Non-Newtonian rheology of leukemic blood and plasma: are n and k parameters of power law model diagnostic? *Physiol Chem Phys Med NMR*. 1992;24(4):307–312.
43. Yavari H, Sadeghi A, Saidi MH, Chakraborty S. Temperature rise in electroosmotic flow of typical non-newtonian biofluids through rectangular microchannels. *J Heat Transfer*. 2014;136(3):031702.
44. Chhabra RP, Richardson JF. *Non-Newtonian Flow and Applied Rheology: engineering Applications*, 2nd ed. Oxford: Butterworth-Heinemann, 2008.
45. Bird RB, Stewart WE, Lightfoot EN. *Transport phenomena*, *2nd ed*. New York: Wiley, 2002.
46. Anderson A, Tannehill JC, Pletcher RH. *Computational Fluid Mechanics and Heat Transfer*. Washington: Hemisphere, 1984.
47. Chien S, Usami S, Taylor HM, Lundberg JL, Gregersen MI. Effects of hematocrit and plasma proteins on human blood rheology at low shear rates. *J Appl Physiol*. 1966;21(1):81–87.
48. Karniadakis G, Beskok A, Aluru N. *Microflows and Nanoflows, Fundamentals and Simulation*. New York: Springer, 2005.
49. Soong CY, Hwang PW, Wang JC. Analysis of pressure-driven electrokinetic flows in hydrophobic microchannels with slip-dependent zeta potential. *Microfluid Nanofluid. 2010;*9(2–3):211–223.

Appendix

The coefficients and functions appeared in the formulation of the problem are given below

$$A_1(x^*,y^*,u^*)=\left[\left(\frac{\partial u^*}{\partial x^*}\right)^2+\left(\frac{\partial u^*}{\partial y^*}\right)^2\right]^{\frac{n-3}{2}}\left[n\left(\frac{\partial u^*}{\partial x^*}\right)^2+\left(\frac{\partial u^*}{\partial y^*}\right)^2\right] \tag{A1}$$

$$A_1(\hat{x},\hat{y},u^*)=\left\{\left[Q_1(\hat{x})\frac{\partial u^*}{\partial \hat{x}}\right]^2+\left[Q_3(\hat{y})\frac{\partial u^*}{\partial \hat{y}}\right]^2\right\}^{\frac{n-3}{2}} \left\{n\left[Q_1(\hat{x})\frac{\partial u^*}{\partial \hat{x}}\right]^2+\left[Q_3(\hat{y})\frac{\partial u^*}{\partial \hat{y}}\right]^2\right\} \tag{A2}$$

$$A_2(x^*,y^*,u^*)=\left[\left(\frac{\partial u^*}{\partial x^*}\right)^2+\left(\frac{\partial u^*}{\partial y^*}\right)^2\right]^{\frac{n-3}{2}}\left[\left(\frac{\partial u^*}{\partial x^*}\right)^2+n\left(\frac{\partial u^*}{\partial y}\right)^2\right] \tag{A3}$$

$$A_2(\hat{x},\hat{y},u^*)=\left\{\left[Q_1(\hat{x})\frac{\partial u^*}{\partial \hat{x}}\right]^2+\left[Q_3(\hat{y})\frac{\partial u^*}{\partial \hat{y}}\right]^2\right\}^{\frac{n-3}{2}} \left\{\left[Q_1(\hat{x})\frac{\partial u^*}{\partial \hat{x}}\right]^2+n\left[Q_3(\hat{y})\frac{\partial u^*}{\partial \hat{y}}\right]^2\right\} \tag{A4}$$

$$A_3(x^*,y^*,u^*)=2(n-1)\left[\left(\frac{\partial u^*}{\partial x^*}\right)^2+\left(\frac{\partial u^*}{\partial y^*}\right)^2\right]^{\frac{n-3}{2}}\frac{\partial u^*}{\partial x^*}\ \frac{\partial u^*}{\partial y^*} \tag{A5}$$

$$A_3(\hat{x},\hat{y},u^*)=2(n-1)Q_1(\hat{x})Q_3(\hat{y})\frac{\partial u^*}{\partial \hat{x}}\frac{\partial u^*}{\partial \hat{y}} \left\{\left[Q_1(\hat{x})\frac{\partial u^*}{\partial \hat{x}}\right]^2+\left[Q_3(\hat{y})\frac{\partial u^*}{\partial \hat{y}}\right]^2\right\}^{\frac{n-3}{2}} \tag{A6}$$

$$Q_1(\hat{x})=\frac{e^{\Omega\hat{x}}+e^{-\Omega\hat{x}}+2}{2\alpha\beta\Omega},\ \ Q_2(\hat{x})=\frac{e^{2\Omega\hat{x}}+2e^{\Omega\hat{x}}-2e^{-\Omega\hat{x}}-e^{-2\Omega\hat{x}}}{4\alpha^2\beta^2\Omega} \tag{A7}$$

$$Q_3(\hat{y})=\frac{e^{\Omega\hat{y}}+e^{-\Omega\hat{y}}+2}{2\beta\Omega},\ \ Q_4(\hat{y})=\frac{e^{2\Omega\hat{y}}+2e^{\Omega\hat{y}}-2e^{-\Omega\hat{y}}-e^{-2\Omega\hat{y}}}{4\beta^2\Omega} \tag{A8}$$

$$Q_5(\hat{z})=\frac{e^{\Omega_z(\hat{z}-1)}+e^{-\Omega_z(\hat{z}-1)}+2}{2L^*\beta_z\Omega_z},$$
$$Q_6(\hat{z})=\frac{e^{2\Omega_z(\hat{z}-1)}+2e^{\Omega_z(\hat{z}-1)}-2e^{-\Omega_z(\hat{z}-1)}-e^{-2\Omega_z(\hat{z}-1)}}{4L^{*2}\beta_z^2\Omega_z} \tag{A9}$$

where,

$$\Omega=\ln\left(\frac{\beta+1}{\beta-1}\right),\ \ \Omega_z=\ln\left(\frac{\beta_z+1}{\beta_z-1}\right) \tag{A10}$$

$$k_{0\psi}=2Q_1^2(\hat{x}_i)\Delta\hat{y}^2+2Q_3^2\left(\hat{y}_j\right)\Delta\hat{x}^2+\kappa^2\Lambda_{i,j}^g\ \Delta\hat{x}^2\Delta\hat{y}^2 \tag{A11}$$

$$k_{1\psi}=Q_1^2(\hat{x}_i)\Delta\hat{y}^2+\frac{1}{2}Q_2(\hat{x}_i)\Delta\hat{x}\Delta\hat{y}^2 \tag{A12}$$

$$k_{2\psi}=Q_1^2(\hat{x}_i)\Delta\hat{y}^2-\frac{1}{2}Q_2(\hat{x}_i)\Delta\hat{x}\Delta\hat{y}^2 \tag{A13}$$

$$k_{3\psi}=Q_3^2\left(\hat{y}_j\right)\Delta\hat{x}^2+\frac{1}{2}Q_4\left(\hat{y}_j\right)\Delta\hat{y}\Delta\hat{x}^2 \tag{A14}$$

$$k_{4\psi}=Q_3^2\left(\hat{y}_j\right)\Delta\hat{x}^2-\frac{1}{2}Q_4\left(\hat{y}_j\right)\Delta\hat{y}\Delta\hat{x}^2 \tag{A15}$$

$$\begin{aligned}k_{0u}=2\Bigg\{&\left[\frac{Q_1(\hat{x}_i)}{\Delta\hat{x}}\right]^2\left\{n[\Delta\hat{y}Q_1(\hat{x}_i)]^2\left(u_{i+1,j}^{*g}-u_{i-1,j}^{*g}\right)^2+\left[\Delta\hat{x}Q_3\left(\hat{y}_j\right)\right]^2\left(u_{i,j+1}^{*g}-u_{i,j-1}^{*g}\right)^2\right\}\\&+\left[\frac{Q_3\left(\hat{y}_j\right)}{\Delta\hat{y}}\right]^2\left\{[\Delta\hat{y}Q_1(\hat{x}_i)]^2\left(u_{i+1,j}^{*g}-u_{i-1,j}^{*g}\right)^2+n\left[\Delta\hat{x}Q_3\left(\hat{y}_j\right)\right]^2\left(u_{i,j+1}^{*g}-u_{i,j-1}^{*g}\right)^2\right\}\Bigg\}\end{aligned} \tag{A16}$$

$$k_{1u}=\left\{n[\Delta\hat{y}Q_1(\hat{x}_i)]^2\left(u_{i+1,j}^{*g}-u_{i-1,j}^{*g}\right)^2+\left[\Delta\hat{x}Q_3\left(\hat{y}_j\right)\right]^2\left(u_{i,j+1}^{*g}-u_{i,j-1}^{*g}\right)^2\right\}\left[\frac{Q_1^2(\hat{x}_i)}{\Delta\hat{x}^2}+\frac{Q_2(\hat{x}_i)}{2\Delta\hat{x}}\right] \tag{A17}$$

$$k_{2u}=\left\{n[\Delta\hat{y}Q_1(\hat{x}_i)]^2\left(u_{i+1,j}^{*g}-u_{i-1,j}^{*g}\right)^2+\left[\Delta\hat{x}Q_3\left(\hat{y}_j\right)\right]^2\left(u_{i,j+1}^{*g}-u_{i,j-1}^{*g}\right)^2\right\}\left[\frac{Q_1^2(\hat{x}_i)}{\Delta\hat{x}^2}-\frac{Q_2(\hat{x}_i)}{2\Delta\hat{x}}\right] \tag{A18}$$

$$k_{3u}=\left\{[\Delta\hat{y}Q_1(\hat{x}_i)]^2\left(u_{i+1,j}^{*g}-u_{i-1,j}^{*g}\right)^2+n\left[\Delta\hat{x}Q_3\left(\hat{y}_j\right)\right]^2\left(u_{i,j+1}^{*g}-u_{i,j-1}^{*g}\right)^2\right\}\left[\frac{Q_3^2\left(\hat{y}_j\right)}{\Delta\hat{y}^2}+\frac{Q_4\left(\hat{y}_j\right)}{2\Delta\hat{y}}\right] \tag{A19}$$

$$k_{4u}=\left\{[\Delta\hat{y}Q_1(\hat{x}_i)]^2\left(u_{i+1,j}^{*g}-u_{i-1,j}^{*g}\right)^2+n\left[\Delta\hat{x}Q_3\left(\hat{y}_j\right)\right]^2\left(u_{i,j+1}^{*g}-u_{i,j-1}^{*g}\right)^2\right\}\left[\frac{Q_3^2\left(\hat{y}_j\right)}{\Delta\hat{y}^2}-\frac{Q_4\left(\hat{y}_j\right)}{2\Delta\hat{y}}\right] \tag{A20}$$

$$k_{5u}=\frac{1}{2}(n-1)\left(u_{i+1,j}^{*g}-u_{i-1,j}^{*g}\right)\left(u_{i,j+1}^{*g}-u_{i,j-1}^{*g}\right)Q_1^2(\hat{x}_i)Q_3^2\left(\hat{y}_j\right) \tag{A21}$$

$$k_{6u}=-(2\Delta\hat{x}\Delta\hat{y})^{n-1}\left\{[\Delta\hat{y}Q_1(\hat{x}_i)]^2\left(u_{i+1,j}^{*g}-u_{i-1,j}^{*g}\right)^2+\left[\Delta\hat{x}Q_3\left(\hat{y}_j\right)\right]^2\left(u_{i,j+1}^{*g}-u_{i,j-1}^{*g}\right)^2\right\}^{\frac{3-n}{2}}\left[\left(\frac{n+1}{n}\right)^n\Gamma+\frac{\mathrm{K}^{n+1}}{n^n\zeta^*}\sinh\psi_{i,j}^*\right] \tag{A22}$$

$$k_{0\Theta}=\Delta\hat{x}^2\Delta\hat{y}^2\Delta\hat{z}^2+2\Delta t^{*p+1}\Delta\hat{y}^2\Delta\hat{z}^2Q_1^2(\hat{x}_i)+2\Delta t^{*p+1}\Delta\hat{x}^2\Delta\hat{z}^2Q_3^2\left(\hat{y}_j\right)+2\Delta t^{*p+1}\Delta\hat{x}^2\Delta\hat{y}^2\frac{Q_5^2(\hat{z}_k)}{Pe^2} \tag{A23}$$

$$k_{1\Theta}=\Delta t^{*p+1}\Delta\hat{y}^2\Delta\hat{z}^2Q_1^2(\hat{x}_i)+\Delta t^{*p+1}\Delta\hat{x}\Delta\hat{y}^2\Delta\hat{z}^2\frac{Q_2(\hat{x}_i)}{2} \tag{A24}$$

$$k_{2\Theta}=\Delta t^{*p+1}\Delta\hat{y}^2\Delta\hat{z}^2Q_1^2(\hat{x}_i)-\Delta t^{*p+1}\Delta\hat{x}\Delta\hat{y}^2\Delta\hat{z}^2\frac{Q_2(\hat{x}_i)}{2} \tag{A25}$$

$$k_{3\Theta}=\Delta t^{*p+1}\Delta\hat{x}^2\Delta\hat{z}^2Q_3^2\left(\hat{y}_j\right)+\Delta t^{*p+1}\Delta\hat{y}\Delta\hat{x}^2\Delta\hat{z}^2\frac{Q_4\left(\hat{y}_j\right)}{2} \tag{A26}$$

$$k_{4\Theta}=\Delta t^{*p+1}\Delta\hat{x}^2\Delta\hat{z}^2Q_3^2\left(\hat{y}_j\right)-\Delta t^{*p+1}\Delta\hat{y}\Delta\hat{x}^2\Delta\hat{z}^2\frac{Q_4\left(\hat{y}_j\right)}{2} \tag{A27}$$

$$k_{5\Theta}=\Delta t^{*p+1}\Delta\hat{x}^2\Delta\hat{y}^2\frac{Q_5^2(\hat{z}_k)}{Pe^2}+\Delta t^{*p+1}\Delta\hat{z}\Delta\hat{x}^2\Delta\hat{y}^2\frac{Q_6(\hat{z}_k)}{2Pe^2}-\Delta t^{*p+1}\Delta\hat{z}\Delta\hat{x}^2\Delta\hat{y}^2\frac{u_{i,j}^*Q_5(\hat{z}_k)}{2} \tag{A28}$$

$$k_{6\Theta}=\Delta t^{*p+1}\Delta\hat{x}^2\Delta\hat{y}^2\frac{Q_5^2(\hat{z}_k)}{Pe^2}-\Delta t^{*p+1}\Delta\hat{z}\Delta\hat{x}^2\Delta\hat{y}^2\frac{Q_6(\hat{z}_k)}{2Pe^2}+\Delta t^{*p+1}\Delta\hat{z}\Delta\hat{x}^2\Delta\hat{y}^2\frac{u_{i,j}^*Q_5(\hat{z}_k)}{2} \tag{A29}$$

$$k_{7\Theta}=\Delta\hat{x}^2\Delta\hat{y}^2\Delta\hat{z}^2\Theta_{i,j,k}^p \tag{A30}$$

Manuscript received Sep. 25, 2014, and revision received Feb. 18, 2015.